Supporting Information

Catalytic Activity and Stability of Oxides: The Role of Near-Surface Atomic Structures and Compositions

Zhenxing Feng[1, 2, 4, *], Wesley T. Hong[1, 3], Dillon D. Fong[5], Yueh-Lin Lee[1 ,2, 6], Yizhak Yacoby[7], Dane Morgan[6], and Yang Shao-Horn[1, 2, 3, *]

[1]*Electrochemical Energy Laboratory,* [2]*Department of Mechanical Engineering,* [3]*Department of Materials Science and Engineering, Massachusetts Institute of Technology, Cambridge, Massachusetts, 02139, USA*

[4]*Chemical Science and Engineering Division,* [5]*Materials Science Division, Argonne National Laboratory, Lemont, Illinois, 60439, USA*

[6]*Department of Materials Science and Engineering, University of Wisconsin—Madison, 1509 University Avenue, Madison, Wisconsin, 53706, USA*

[7]*Racah Institute of Physics, Hebrew University, Jerusalem, 91904, Israel*

[*]Corresponding author (e-mail: z-feng@u.northwestern.edu; shaohorn@mit.edu)

Index **Page**

Supplementary Methods

Coherent Bragg Rod Analysis (COBRA) and Differential COBRA.

The COBRA technique is based on measurements of the diffraction intensities along substrate-defined crystal truncation rods (CTRs). It starts with a reference structure representing the idealized film structure as well as the underlying single crystal substrate structure and then uses an iterative phasing algorithm to converge upon the true electron density. COBRA differs from other phasing algorithms in that it uses the approximation that at two adjacent points along the Bragg rod, the change in the complex structure factors (CSFs) contributed by the unknown part of electron density are small compared to the change in CSFs contributed from the known structure (typically the single-crystal substrate).[1] COBRA, combined with the difference map method,[2] allows retrieval of the CSFs (including the amplitudes and phases) along the Bragg rods; the Fourier transform of the CSFs into real space give the 3D electron density of the so-called "folded structure" of the film and substrate. The folded structure is obtained by laterally translating each atom in the film and the top layers of the substrate to one substrate-defined two dimensional (2D) unit cell using substrate-defined 2D (*i.e.*, in-plane) unit cell vectors. As a result, while the 3D through-thickness structure of epitaxial films can be reconstructed, the phases of atoms with no average registry with the substrate are not resolved. Good agreement between the measured intensities and the electron density-based calculated intensities can be attained even after only a few COBRA iterations. An example of a COBRA-determined electron density (EDY) for a thin film heterostructure is shown in Figure 2(a). As seen, COBRA is a powerful tool for providing sub-Å resolution structural information in epitaxial thin films (as well as epitaxial quantum dots).

By analyzing the 3D EDY one can obtain important information on the system, such as atomic positions and occupations of elements. The error bars of the parameters of interest, such as the apical oxygen positions, have been estimated for each individual sample using the following method, referred to as Uncertainty Analysis. This method resembles the widely used Bootstrap resampling approach for uncertainty estimations in statistical analysis.[3]

Furthermore, element-specific structural information can be determined by performing additional anomalous scattering measurements that exploit the energy-dependence of elemental scattering cross-sections to obtain a differential signal that depends on an element's spatial distribution. This comprises the energy-modulated differential COBRA technique and provides the resolution needed to determine atomic concentrations on individual crystallographic sites, as shown in Figure 2b. Differential COBRA[4] uses the energy-dependence of the elemental scattering cross-sections. At each point along the rods the difference between the diffraction intensities is measured just below and just above the absorption edge of the element of interest. The main sources of error in measuring the diffraction intensities are systematic, coming from uncertainties in the background subtraction and from errors in determining the position along the Bragg rod and the diffraction phases: the advantage of the differential method is to significantly reduce the systematic errors, thus increasing the accuracy of the measured difference. If the

entire data set is measured and analyzed at one energy at a time, these errors are largely independent and propagate, resulting in increased uncertainty.[5] On the other hand, if the diffraction intensity is measured differentially, i.e. if one measures the difference in the diffraction intensities at the two energies at each point along the Bragg rod, the errors are partially canceled and the uncertainty is decreased.

Using COBRA along with the difference map, the effective EDY, $\rho_L = \rho(x, y, z)$, can be determined from the full data set measured at the lower energy. The EDY can then be used to calculate the diffraction intensity $I_L(h, k, l)$ along the different rods. At the higher energy, due to the change in the complex scattering factor, the effective EDY will change to

$$\rho_H = \rho_L + \sum_i \rho_i^A(x_i, y_i, z_i) c_i^A \Delta f_A, \qquad \text{Eq. (S1)}$$

$$\text{where } \hat{\rho}_i^A = \frac{\hat{\rho}_i}{f_A^r + f_o \Phi(\vec{k})},$$

$\hat{\rho}_i$ is the Fourier transform of the electron density ρ_i around site i, f_A^r, f_o are the real part of the anomalous and the ordinary scattering cross-sections at the low energy, respectively, and $\Phi(\vec{k})$ is the three dimensional atomic form factor of selected cation (Sr in this case) normalized to unity at $k = 0$; c_i^A is the fraction of the electrons close to site i that belong to Sr and Δf_A is the difference between the complex anomalous scattering factors of Sr at the higher and lower energies.. The change in the EDY, $\Delta\rho$, results in a change in the diffraction intensities, $I_H(h, k, l) = I_L(h, k, l) + \Delta I$. The only unknowns are the c_i^A 's thus, by refining the c_i^A parameters, ΔI can be fitted to the measured differential signal, which allows us to determine the individual occupancies of the probe atom within the folded unit cell.

Determining the phases of coherent materials using COBRA.

For $(La_{1-y}Sr_y)_2CoO_{4\pm\delta}/La_{1-x}Sr_xCoO_{3-\delta}$ ($LSCO_{214}/LSCO_{113}$) heterostructured system, Figure S5 shows electron densities (EDY)s along (a) the (0,0,Z) line that passes through (La,Sr) atoms in $LSCO_{113}$ and (La,Sr)/Co/O_I in $LSCO_{214}$, and (b) the (0.5,0.5,Z) line that passes through Co/Ti/O_I atoms in $LSCO_{113}$ and (La,Sr)/Co/O_I in $LSCO_{214}$. It should be noted that the stacking sequence for atoms along (0,0,Z) is A - □ - A - □ - A for perovskite and A - □ - A – O – B – O … for Ruddlesden-Popper (RP), while along (0.5,0.5,Z) the sequence is O – B – O – B for perovskite and O – B – O – A - □ - A for RP. All atoms and their positions can be clearly identified in the EDY plot, including oxygen, except those at the very surface of the film. The interface of $LSCO_{214}$-on-$LSCO_{113}$ can also be clearly identified, and the atomic structures are consistent with the previous STEM observation.[6] The small EDY fluctuations between peaks shown in Figure S5 provide a measure of the EDY uncertainty,[3,7] which is generally smaller than the oxygen EDY.

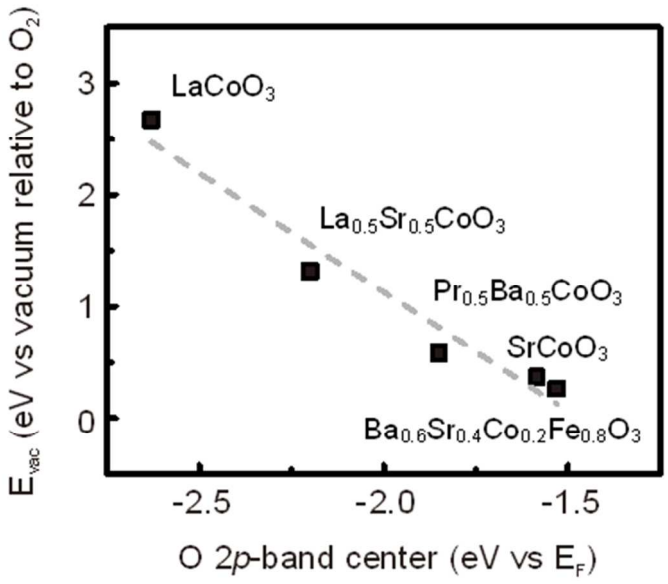

Figure S1. Enthalpy of formation of an oxygen vacancy compared to the oxygen 2*p*-band center relative to the Fermi level for $LaCoO_3$, $La_{0.5}Sr_{0.5}CoO_3$, $Pr_{0.5}Ba_{0.5}CoO_3$, $SrCoO_3$, and $Ba_{0.6}Sr_{0.4}Co_{0.2}Fe_{0.8}O_3$ with full oxygen stoichiometry, showing the correlation existing between oxygen vacancy formation energetics and the oxygen 2*p*-band center relative to the Fermi level.

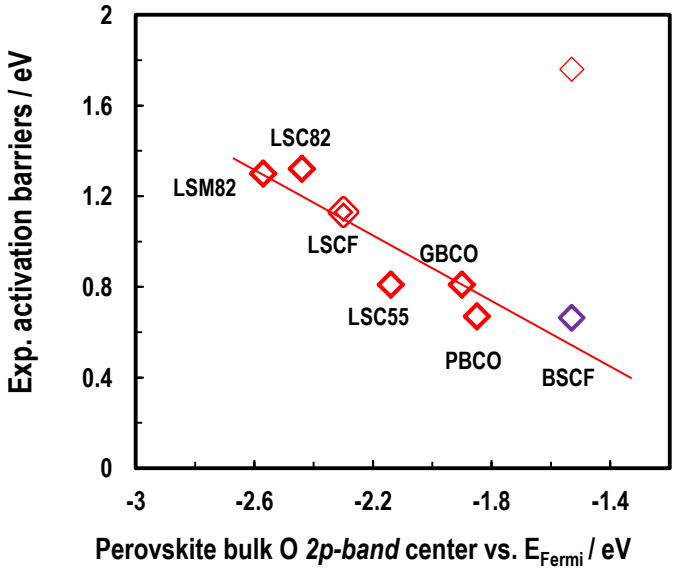

Figure S2. The experimental activation barriers (ΔE_a) for k_O* (red empty diamonds) summarized in Table 1 of Ref. 8 for $La_{0.8}Sr_{0.2}MnO_{3+\delta}$ (LSM82), $La_{0.8}Sr_{0.2}CoO_{3-\delta}$ (LSC82), $La_{0.5}Sr_{0.5}CoO_{3+\delta}$ (LSC55), $GdBaCo_2O_{6-\delta}$ (GBCO), $PrBaCo_2O_{6-\delta}$ (PBCO), and $Ba_{0.5}Sr_{0.5}Co_{0.8}Fe_{0.2}O_{3-\delta}$ (BSCF) *vs.* the computed bulk O *2p*-band centers collected from the previous works[9,10] (LSC55 from Ref. 10). Figure S2 is reproduced from Lee *et al.*[11]

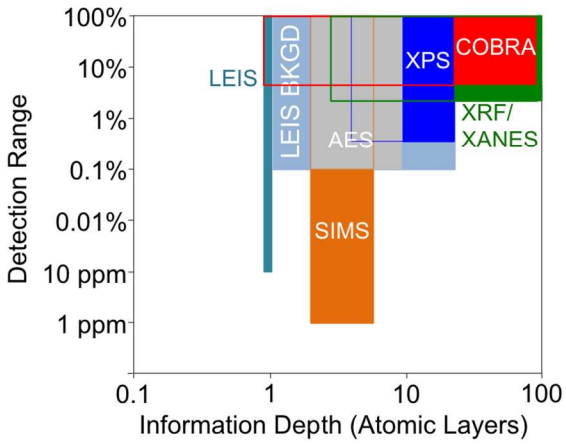

Figure S3. A detailed comparison of the detection limits and the information depths of several surface analytical techniques mentioned in this Review. For example, low energy ion scattering (LEIS) is sensitive to detect the surface outer atomic layer with wide detection range for elements, namely, from 10 ppm concentration up to completed coverage. LEIS background (BKGD) has wider information depth but less sensitivity in element concentration.

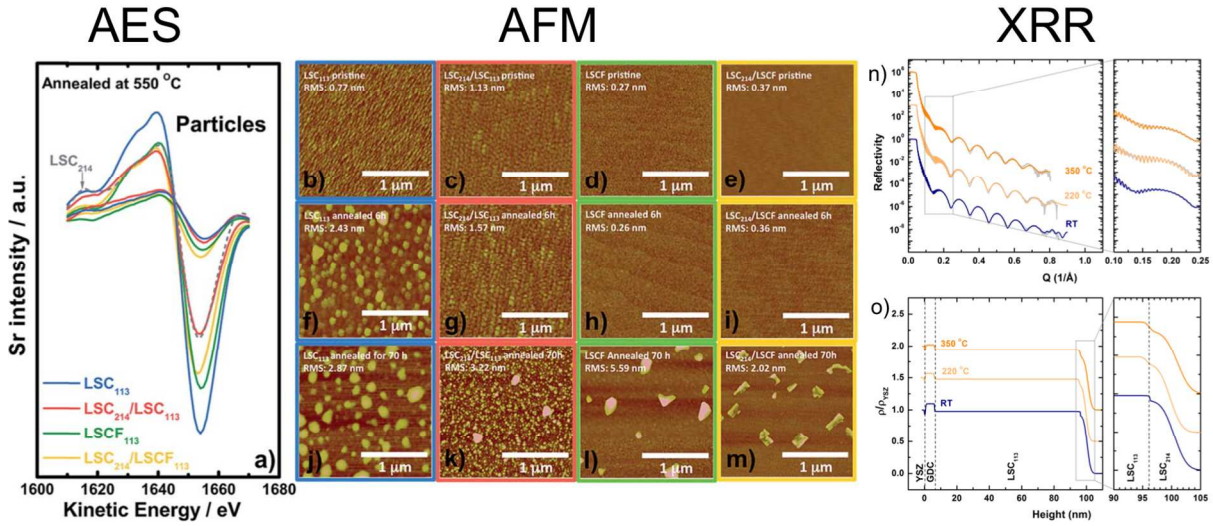

Figure S4. Auger electron spectra (AES) and atomic force microcopy (AFM) images for bare LSC_{113}, $LSCF_{113}$ and LSC_{214}-decorated LSC_{113} and LSC_{214}-decorated $LSCF_{113}$ thin films. (a) Sr Auger spectra for: LSC_{113} (blue), LSC_{214}-decorated LSC_{113} (red), $LSCF_{113}$ (green), and LSC_{214}-decorated $LSCF_{113}$ (yellow) after annealing at 550 °C for 70 hours at an oxygen pressure of 1 atm. The dashed gray line is the Sr spectrum of a pristine LSC_{214} reference sample. The peak-to-peak values in Auger spectra reflect the Sr concentrations. AFM images of as-deposited (b) LSC_{113}, (c) LSC_{214}-decorated LSC_{113}, (d) $LSCF_{113}$, and (e) LSC_{214}-decorated $LSCF_{113}$. The AFM image shows particle formation on (f) 6 h annealed LSC_{113} but no particles were observed on (g) 6 h annealed LSC_{214}-decorated LSC_{113}, (h) 6 h annealed LSC_{214}-decorated LSC_{113}, and (i) 6 h annealed LSC_{214}-decorated LSC_{113}. After annealing for 70 h, particles were observed on all surfaces; (j) annealed LSC_{113}, (k) annealed LSC_{214}-decorated LSC_{113} (l) annealed $LSCF_{113}$ and (m) annealed LSC_{214}-decorated $LSCF_{113}$. (n) *In situ* X-ray reflectivity (XRR) data and fits of 4 nm $(La_{0.5}Sr_{0.5})_2CoO_{4+\delta}$ (LSC_{214}) decorated 90 nm LSC_{113}/GDC/YSZ at different temperatures: room temperature (RT), 200 °C, and 350 °C in ambient air. (o) The EDY obtained from the fits of the XRR data. Particles (observed from AFM) show different Sr segregation (from AES) for LSC_{214}-decorated LSC_{113} is supported by XRR in its surface electron density profile in (o).

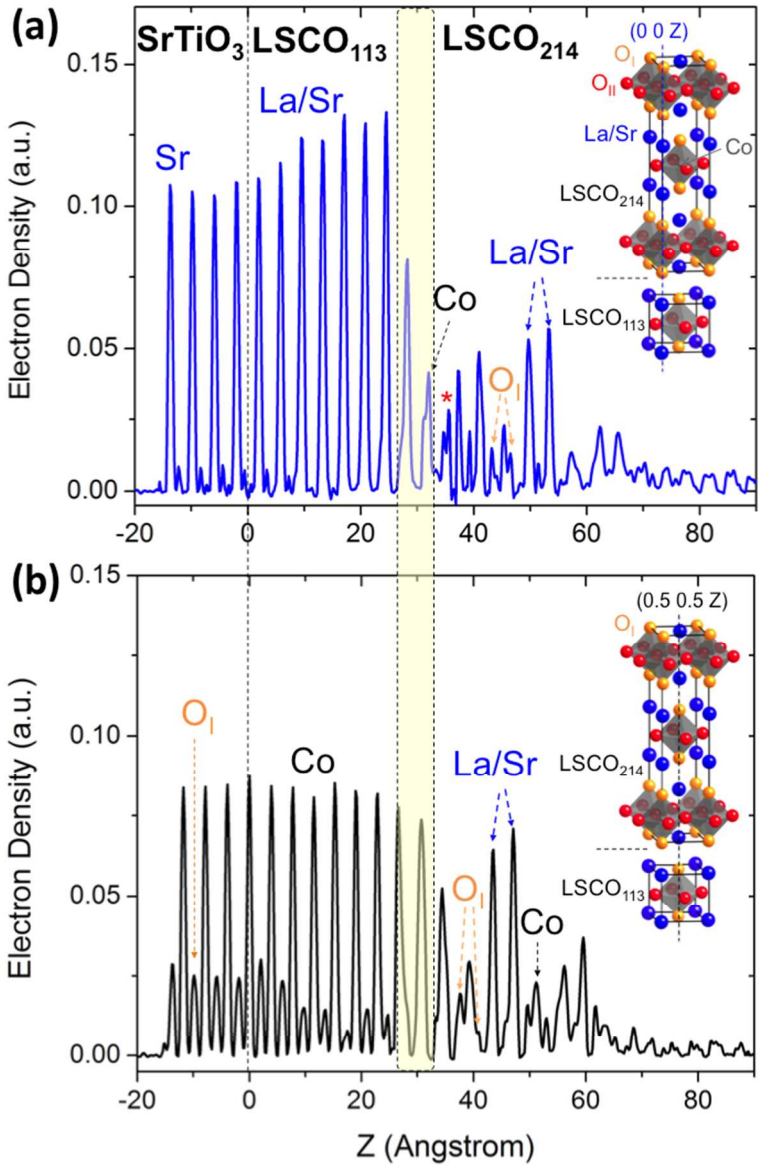

Figure S5. The COBRA-determined electron density (EDY) of as-deposited $LSCO_{214}/LSCO_{113}$/STO along: (a) the (0 0 Z) line; (b) the (0.5 0.5 Z) line. Clearly the structure of $LSCO_{214}$ and $LSCO_{113}$ can be distinguished, as the La/Sr layer ordering is different. $LSCO_{214}$ has two adjacent La/Sr layers, while $LSCO_{113}$ has alternated La/Sr and CoO_2 layers.

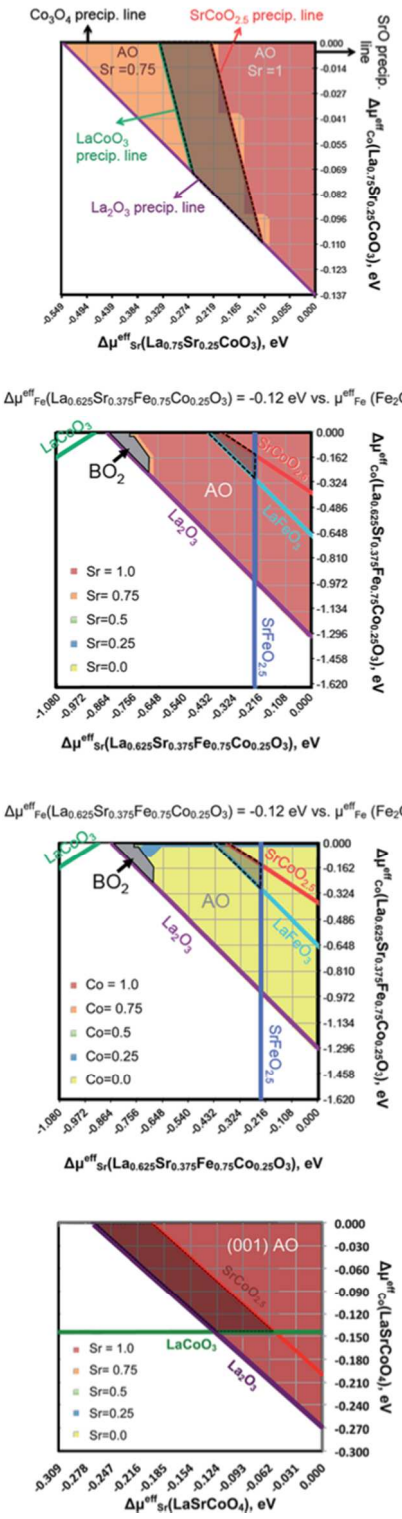

Figure S6. (a) is the predicted $La_{0.75}Sr_{0.25}CoO_3$ surface stability diagram at T = 550 °C and $p(O_2)$ = 1 atm based on the effective metal chemical potentials of bulk $La_{0.75}Sr_{0.25}CoO_3$. The grid points represent the sampled bulk effective chemical potentials of Sr (x-axis; x = 0 represents the equilibrium between $La_{0.75}Sr_{0.25}CoO_3$ and SrO) and Co (y-axis; y = 0 represents the equilibrium between $La_{0.75}Sr_{0.25}CoO_3$ and Co_3O_4) in $La_{0.75}Sr_{0.25}CoO_3$, and the contour plot beyond the grid is constructed based on the calculated lowest surface energy among the investigated $La_{0.75}Sr_{0.25}CoO_3$ (001) surface configurations. The shaded area within dotted lines represents the $La_{0.75}Sr_{0.25}CoO_3$ bulk stable region relative to the lower order oxide compounds ($LaCoO_3$–green, $SrCoO_{2.5}$–red, La_2O_3–purple, SrO–x = 0, and Co_3O_4–y = 0). $La_{0.75}Sr_{0.25}CoO_3$ (001) surface stability analysis results suggest that the most stable surfaces are the AO surfaces with the surface layer A-site Sr concentration equal to 0.75 within the bulk stable region relative to the lower order oxide compounds. (b and c) are the predicted $La_{0.625}Sr_{0.375}Fe_{0.75}Co_{0.25}O_3$ (001) top two surface layer Sr and Co compositions at T = 550 °C and $p(O_2)$ = 1 atm under the condition $\Delta\mu^{eff}_{Fe}(La_{0.625}Sr_{0.375}Fe_{0.75}Co_{0.25}O_3)$ = 0.12 eV *vs.* $\Delta\mu^{eff}_{Fe}(Fe_2O_3)$. The grid points represent the sampled bulk effective chemical potentials of Sr (x-axis; x = 0 represents the equilibrium between $La_{0.625}Sr_{0.375}Fe_{0.75}Co_{0.25}O_3$ and SrO) and Co (y-axis; y = 0 represents the equilibrium between $La_{0.625}Sr_{0.375}Fe_{0.75}Co_{0.25}O_3$ and Co_3O_4) in $La_{0.625}Sr_{0.375}Fe_{0.75}Co_{0.25}O_3$. The effective chemical potential conditions, in which the BO_2 surface is more stable than the AO are presented by the grey area. The shaded area within dotted lines in (b and c) represents the $La_{0.625}Sr_{0.375}Fe_{0.75}Co_{0.25}O_3$ bulk stable region relative to the lower order oxides ($LaFeO_3$–light blue, $SrFeO_{2.5}$–deep blue, $LaCoO_3$–green, $SrCoO_{2.5}$–red, La_2O_3–purple, SrO–x = 0, and Co_3O_4–y = 0). The $La_{0.625}Sr_{0.375}Fe_{0.75}Co_{0.25}O_3$ (001) surface stability analysis results suggest that the most stable surfaces are the AO surfaces with the surface layer A-site Sr concentration equal to 1.00 and such conclusion holds for all the other investigated conditions of ($La_{0.625}Sr_{0.375}Fe_{0.75}Co_{0.25}O_3$), including $\Delta\mu^{eff}_{Fe}(La_{0.625}Sr_{0.375}Fe_{0.75}Co_{0.25}O_3)$ = 0.0, -0.24, and -0.36 eV *vs.* $\Delta\mu^{eff}_{Fe}(Fe_2O_3)$. (d) are the predicted contour plots for the $LaSrCoO_4$ stable (001) *vs.* (100) surface layer compositions within the bulk $LaSrCoO_4$ stability boundaries (in equilibrium with La_2O_3, SrO, Co_3O_4, $LaCoO_3$, and $SrCoO_{2.5}$) based on the most stable surface energy of the investigated six $LaSrCoO_4$ (001) and (100) slab configurations *vs.* chemical potentials of Sr (relative to SrO) and Co (relative to Co_3O_4) at T = 550 °C and $p(O_2)$ = 1 atm. The shaded region represents the stable bulk $LaSrCoO_4$. For the same surface orientation, both the (001) AO and the (100) A_2BO_4 surfaces are predicted to be stable with fully enriched surface layer Sr at the A-sites. Comparatively, the surface energy of the fully Sr-enriched (100) A_2BO_4 surface is found to be a factor of 1.2–2 with respect to the surface energy of the fully Sr-enriched (001) AO surface within the stable bulk $LaSrCoO_4$ region, suggesting the greater stability of the (001) AO surface with fully enriched Sr vs. the (100) A_2BO_4 surfaces.

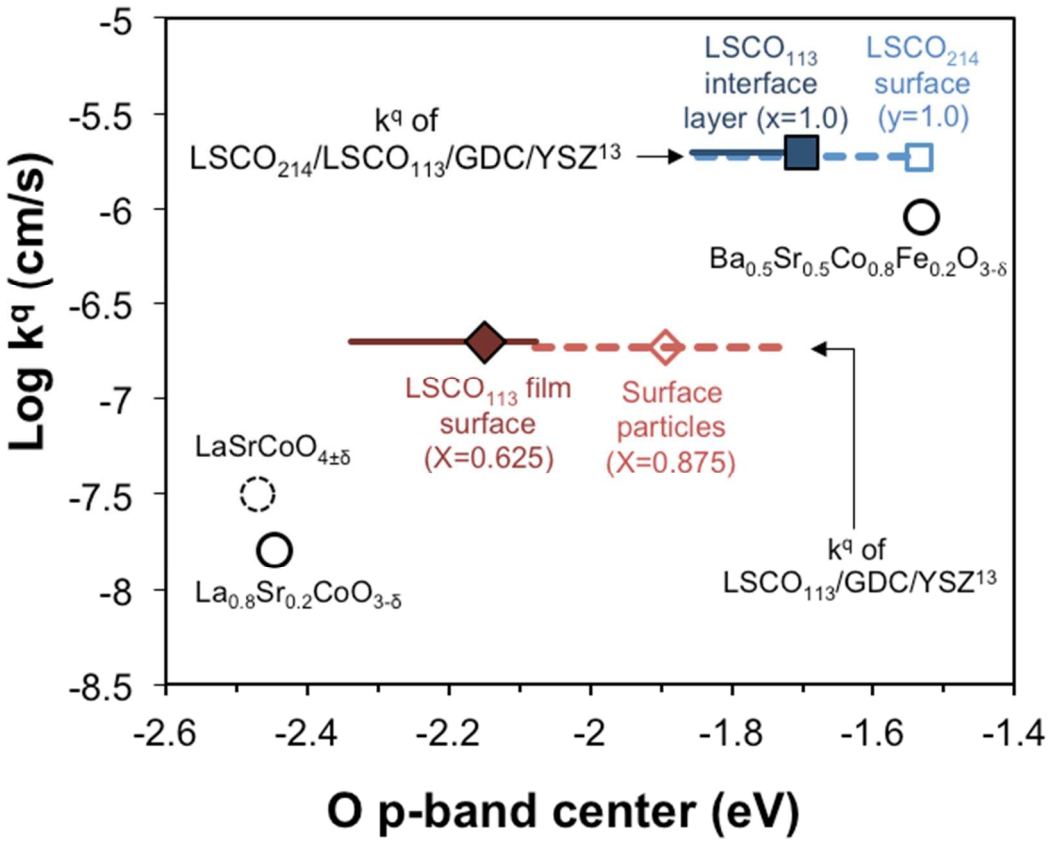

Figure S7. The figure shows surface exchange coefficients k^q or k^* vs. the calculated O 2*p* band centers (relative to the Fermi level) calculated for bulk unit cells. The specific details for each data point are as follows. k^q values are shown for uncoated $La_{0.8}Sr_{0.2}CoO_{3-\delta}$ films ($LSCO_{113}$, red diamonds) and $(La_{0.5}Sr_{0.5})_2CoO_{4\pm\delta}$ ($LSCO_{214}$, blue squares) covered $LSCO_{113}$ films, both on the yttria-stabilized zirconia (001) single crystals buffered by a gadolinium-doped ceria layer at T= 550 °C, $P(O_2)$= 1 bar[13]. Each of these cases has associated with two separate O 2*p* band center values corresponding to two possible compositions used in the bulk calculations for each case, which compositions are estimated from COBRA measurements of the most relevant active surface or interface layers. Although the compositions are estimated from surface or interface compositions, the O 2*p* band center calculations are done with bulk unit cells. The possible error in the COBRA measurement for the Sr occupancy (~10%) is represented by the thin horizontal bars. Adapted with permission from Ref. 10. Copyright 2014, American Chemical Society.

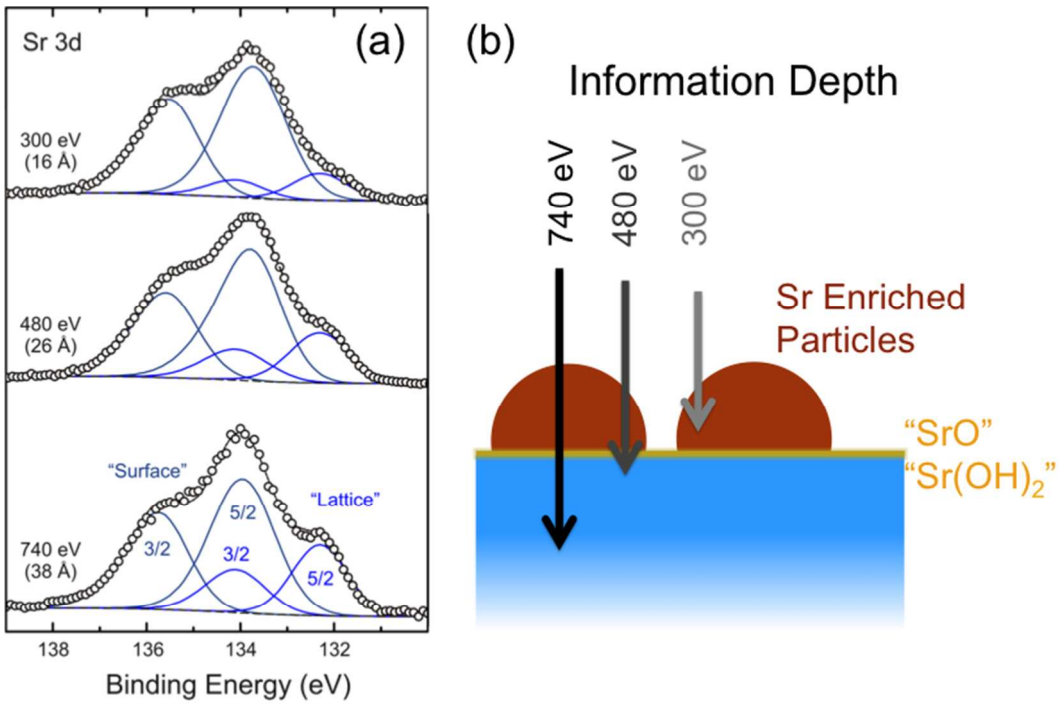

Figure S8. Summary of surface chemistry studies on $La_{0.8}Sr_{0.2}CoO_{3-\delta}$ thin films. (a) APXPS Sr 3d spectra of 85 nm $La_{0.8}Sr_{0.2}CoO_{3-\delta}$ film grown on yttria-stabilized zirconia at 370 °C in 760 mTorr O2. Distinct "surface" and "lattice" components were resolved using differential energy depth-profiling. The binding energy of the "surface" component has been attributed to Sr-enriched secondary phases such as SrO and $Sr(OH)_2$, as well as a Sr-segregated phase such as $Sr_2Co_2O_5$ as illustrated in (b).

References

(1) Sowwan, M.; Yacoby, Y.; Pitney, J.; MacHarrie, R.; Hong, M.; Cross, J.; Walko, D. A.; Clarke, R.; Pindak, R.; Stern, E. A. Direct atomic structure determination of epitaxially grown films: Gd_2O_3 on GaAs(100). *Phys. Rev. B* **2002**, *66*, 205311.

(2) Elser, V. Solution of the crystallographic phase problem by iterated projections. *Acta. Crystallogr. A* **2003**, *59*, 201-209.

(3) Zhou, H.; Pindak, R.; Clarke, R.; Steinberg, D. M.; Yacoby, Y. The limits of ultrahigh-resolution x-ray mapping: estimating uncertainties in thin-film and interface structures determined by phase retrieval methods. *J Phys D Appl Phys* **2012**, *45*, 195302.

(4) Yacoby, Y.; Zhou, H.; Pindak, R.; Bozovic, I. Atomic-layer synthesis and imaging uncover broken inversion symmetry in $La_{2-x}Sr_xCuO_4$ films. *Phys. Rev. B* **2013**, *87*, 014108.

(5) Kumah, D. P.; Shusterman, S.; Paltiel, Y.; Yacoby, Y.; Clarke, R. Atomic-scale mapping of quantum dots formed by droplet epitaxy. *Nat. Nanotechnol.* **2009**, *4*, 835-838.

(6) Crumlin, E. J.; Mutoro, E.; Ahn, S. J.; la O', G. J.; Leonard, D. N.; Borisevich, A.; Biegalski, M. D.; Christen, H. M.; Shao-Horn, Y. Oxygen Reduction Kinetics Enhancement on a Heterostructured Oxide Surface for Solid Oxide Fuel Cells. *J. Phys. Chem. Lett.* **2010**, *1*, 3149-3155.

(7) Zhou, H.; Yacoby, Y.; Butko, V. Y.; Logvenov, G.; Bozovic, I.; Pindak, R. Anomalous expansion of the copper-apical-oxygen distance in superconducting cuprate bilayers. *P. Natl. Acad. Sci. USA* **2010**, *107*, 8103-8107.

(8) Tarancon, A.; Burriel, M.; Santiso, J.; Skinner, S. J.; Kilner, J. A. Advances in Layered Oxide Cathodes for Intermediate Temperature Solid Oxide Fuel Cells. *J. Mater. Chem.* **2010**, *20*, 3799-3813.

(9) Lee, Y.-L.; Kleis, J.; Rossmeisl, J.; Shao-Horn, Y.; Morgan, D. Prediction of Solid Oxide Fuel Cell Cathode Activity with First-Principles Descriptors. *Energ. Environ. Sci.* **2011**, *4*, 3966-3970.

(10) Feng, Z.; Yacoby, Y.; Gadre, M. J.; Lee, Y.-L.; Hong, W. T.; Zhou, H.; Biegalski, M. D.; Christen, H. M.; Adler, S. B.; Morgan, D.; Shao-Horn, Y. Anomalous Interface and Surface Strontium Segregation in $(La_{1-y}Sr_y)_2CoO_{4\pm\delta}/La_{1-x}Sr_xCoO_{3-\delta}$ Heterostructured Thin Films. *J. Phys. Chem. Lett.* **2014**, *5*, 1027-1034.

(11) Lee, Y. L.; Lee, D.; Wang, X.; Lee, H. N.; Morgan, D.; Shao-Horn, Y. Kinetics of Oxygen Surface Exchange on Epitaxial Ruddlesden-Popper-Type (001) Oriented Thin Films and Correlations to First-Principles Descriptors. *J. Phys. Chem. Lett.* **2015**, *7*, 244-249.